This is a post-peer-review, pre-copyedit version of an article published in Mathematical Geosciences. The final authenticated version is available online at: https://doi.org/10.1007/s11004-021-09965-7

Stochastic modelling of sub-seismic faults conditioned on displacement and orientation maps

Håvard Goodwin[1*] - Eyvind Aker[1] - Per Røe[1]

Received: 29 January 2021 / Accepted: 11 July 2021

Abstract: Sub-seismic faults are small faults or fractures that may be difficult to determine but can have large consequences on fluid flow and pressure communication in the subsurface. Thus, knowing their distributions may be important in several subsurface applications, like hydrocarbon exploration and exploitation, geothermal energy production and subsurface CO_2 injection. The aim of the presented work is to use a stochastic model to populate a three-dimensional structural model of the subsurface with sub-seismic faults. The novelty of the proposed method is to condition the stochastic model to input maps describing displacement and stress orientation along subsurface horizons. Hence, the resulting structural model will be consistent with these maps. The maps can originate from a variety of sources, for example from predictions of a geomechanical model or (indirect) measurements of subsurface displacements and stresses. The model uses the optimization algorithm simulated annealing, where the residual between the displacement of the modelled sub-seismic faults and the input displacement map is minimized in an iterative process. Each sub-seismic fault is modelled with a three-dimensional displacement field around the fault slip plane, making comparisons to the input displacement [1]map along a horizon possible. An example of how the model distributes the sub-seismic faults around larger known faults, using a synthetically created displacement map, is provided. The result shows that the model quickly converges towards a set of sub-seismic faults giving total displacement and strike orientation close to the input maps.

[*]*Corresponding author (e-mail: havard.goodwin@nr.no)*

[1] Norwegian Computing Center. P.O. Box 114 Blindern, NO-0314 Oslo, Norway

Keywords: Sub-seismic faults, structural model, stochastic modelling, displacement maps, simulated annealing

1. Introduction

Sub-seismic faults are small faults or fractures that are not visible on seismic data and poorly sampled in wells (Yielding et al. 1992). Larger faults with throws above the limit of seismic resolution can be interpreted from seismic data. High resolution seismic and advanced interpretation techniques like fault attribute volumes can map faults with throws less than 10 meters (Torabi et al. 2019a; Roche et al. 2021), whereas lower resolution seismic may only resolve faults with throws above 20-30 meters (Maerten et al. 2006). In the range between the sub-seismic and the larger faults, only a fraction of the true number of faults may be interpreted from seismic (Bond 2015).

Sub-seismic faults can have large consequences on fluid flow and pressure communication in the subsurface and modelling their effect may be important in assessing natural resources (Yielding et al. 1992; Damsleth et al. 1998). In hydrocarbon production, the sub-seismic faults may affect the production performance and is important for field development strategies and production forecasts. In other applications like geologic storage of CO_2 or geothermal energy production, they may have impact on the reservoir potential and fluid flow paths with respect to storage capacity and energy production.

Structural modelling of sub-seismic faults is an uncertain exercise and several methods to generate fault networks is proposed in the literature. Munthe et al. (1994) proposes a stochastic clustering and repulsion technique dividing faults into mother and children groups. Furthermore, they argue to perform the fault modelling on unfaulted horizons to avoid mismatch between modelled horizons (with faults) and the seismically observed horizons. Following their work, Hollund et al. (2002)

specifies the location of the mother and children faults based on fault density maps indicating regions more likely to have sub-seismic faults than others. In Maerten et al. (2006) the fault density maps are estimated from subsurface stresses near larger observed faults. The stresses are obtained from a geomechanical simulator and combined with a Coulomb failure criterion they predict orientation and densities of the smaller faults. Sub-seismic faults that displaces the horizons more than a tolerated distance away from their seismically observed positions are excluded. The same approach is adopted in Gong et al. (2018). The fault network can alternatively be created using a fault growth algorithm tied to a heuristic geomechanical model like in Gillespie et al. (2017) and references therein. Others addresses the uncertainty in the structural interpretation of faults and how to stochastically perturb the topology and the geometry of the fault network. For example, Godefroy et al. (2019) suggests a theoretical framework of using graph theory and geological rules and Cherpeau (2010) proposes to represent the topology of the fault network by binary threes. The latter is based on the idea of a fault operator like Hollund et al. (2002), but is more flexible and not restricted to corner-point reservoir grids used for flow simulations (Ponting 1989).

The approach presented here is to stochastically generate sub-seismic faults conditioned on displacement and strike orientations maps. The fault model is similar to Hollund et al. (2002), and the fault attributes (displacement, geometry and orientation) are stochastically modelled according to statistical distributions, an approach first proposed by Yielding et al. (1992). The sub-seismic faults are elliptically shaped with a surrounding three-dimensional displacement field as described in Georgsen et al. (2012). The displacement along the fault surface represents the fault throw. The influence of all faults at any given point in the volume can be calculated and defines the total three-dimensional displacement field. The total displacement field is compared to the input displacement map along a horizon. The stochastic optimization framework of simulated annealing (Kirkpatrick 1983) is used for the comparison, where an iterative process stochastically updates faults to improve the match between the total displacement field and the input displacement map.

The total displacement field can be seen as a measure of the continuous fault-induced strain and can thus be compared to displacement maps based on strain calculations from geomechanical modelling. The suggested approach can therefore be useful in applications where geomechanical predictions or (indirect) measurements of subsurface displacement and stresses are available. Another advantage is that the applied fault model works directly on a corner-point reservoir grid used for flow simulations. Hence, it can be included in a workflow assessing the effect different networks have on the fluid flow. Simulated annealing has previously been applied to fracture modelling. For example, Tran et al. (2006) applies it to model discrete fracture networks where the function they optimize (the object function) is an average of functions describing different fracture statistics. Masihi et al. (2012) and Mahmoodpour and Masihi (2016) uses a more physical approach with an object function based on mechanical equilibrium between fracturing and strain energy. The novelty of the presented algorithm is to tie the object function to the residual between the displacement of the generated fault set and the input map. The residual is calculated along a horizon and uses the modelled displacement field around of each sub-seismic fault in the network.

The functionality of the algorithm is demonstrated on synthetically created displacement and orientation maps. The result shows that the algorithm quickly converges towards a set of sub-seismic faults giving total displacement and strike orientation close to the synthetic maps. The robustness of the algorithm is also tested by applying different fault size distributions and compare the results.

The focus of this paper is on the stochastic optimization algorithm and its mathematical framework. The paper is outlined as follows: Sect. 2 describes the fault model and Sect. 3 presents the optimization algorithm. The example and results are given in Sect. 4. The model and results are discussed in Sect. 5, and lastly summarized in Sect. 6.

2. Stochastic Fault Model

The fault model is constructed by three-dimensional operators, which means it is not only the fault surface that is modelled, but also how the faulting influences and deforms the surrounding volume (Georgsen et al. 2012). A typical fault in a gridded surface is illustrated in Fig. 1 where the volume around the slip surface is deformed within the influence range. The range defines the influence radius for the deformation around the fault surface. One advantage with the deformation operator is that it can be reversed, thus faults and their effects on the surrounding volume can also be removed from the geometry (Hollund et al. 2002). With this model it is possible to add and remove faults individually and update the total displacement field accordingly. This is essential when faults are added and removed stochastically in the optimization algorithm. The sub-seismic faults are modelled as ellipses with maximum displacement at the center and an ellipsoidal volume of influence around the fault (Hollund et al. 2002; Gibson et al. 1989).

The fault model enables modelling of fault sets that are distributed in a three-dimensional volume following a marked point process (Munthe et al. 1994). A marked point process is a process where points are first distributed in a volume, and then each point gets associated marks assigned to it. The marks can be any feature and can be stochastically drawn. Here the fault center points are the distributed points in the volume, and the marks are the fault attributes, that is maximum displacement, length, height, range, strike and dip angle.

For each fault, the maximum displacement d is drawn from a truncated power-law distribution

$$g(d) = \frac{Kd^{-K-1}}{d_{min}^{-K} - d_{max}^{-K}}, \tag{1}$$

where $g(d)$ is the probability density, $K > 0$ is the power-law exponent and d_{min} and d_{max} are the truncation limits of the distribution.

The length, height and range of each fault are drawn from subsequent distributions using the drawn d as an input parameter, similar to Hollund et al. (2002) and Munthe et al. (1994). The distributions for the fault attributes length (l), height (h) and range (r) are

$$l = \left(\frac{d}{c_1}\right)^{\frac{1}{c_2}} V_1,\ h = \frac{l}{c_3} V_2,\ r = c_4 \sqrt{lh} V_3, \tag{2}$$

where, $c_1, \dots, c_4$ are constant positive parameters and V_1, V_2, V_3 are log-normal distributions representing the noise in the model. A log-normal distribution is a probability distribution where the logarithm of the variable is normally distributed. This ensures that the drawn random values are positive, giving meaningful fault attributes from the relations in Eq. (2). The log-normal distributions V_1, V_2, V_3 are defined with expectation equal to 1 and user defined standard deviations $\sigma_1, \sigma_2, \sigma_3$. The constant parameters $c_1, \dots, c_4$ and the standard deviations $\sigma_1, \sigma_2, \sigma_3$ can be estimated from seismically mapped faults or geological outcrop data. See for example Walsh and Watterson (1988) and Kim and Sanderson (2005) for discussions on relationships between displacement and dimension attributes of faults.

According to Munthe et al. (1994) the marked point process is defined as follows:

1. Draw the coordinates of the center point of the sub-seismic fault.
2. Draw the maximum displacement from a power-law distribution using Eq. (1).
3. Draw the dimension attributes of the sub-seismic fault using Eq. (2).
4. Draw the orientations (strike and dip).

The marked point process is used to generate a specific number of faults within a volume. The position (coordinates) of the faults may be drawn uniformly or they can be drawn based on density maps where some regions will be more populated with faults than others.

The strike and dip of the faults are drawn from normal distributions with specified means and standard deviations. Mixture of different normal distributions creating a multimodal distribution of, for example, strike orientation is possible. The mean value of the distributions may also be drawn from maps causing them to vary laterally. See Fig. 2 for examples of faults where the position is drawn either uniformly in a volume, or from lateral varying maps.

3. Optimization Algorithm

The optimization algorithm follows the framework of simulated annealing (Kirkpatrick 1983). The aim is to minimize an object function, that is the residual distance between the displacement field of the generated fault set and the displacement map. The starting point is an initial fault set (of n faults) generated using the marked point process. For every iteration the algorithm selects one fault in the current fault set at random and samples a new proposed fault. The total displacement field is calculated for both the current fault set and a new proposed fault set where the selected fault is replaced with the proposed fault. If the proposed fault set has lower residual distance, it is kept and the current fault set is discarded.

One key aspect of the algorithm is that it sometimes accepts the proposed fault set even if it causes an increase in the (residual) distance. This is done to avoid local minima. How likely it is to accept such a set depends on how much the proposed fault increases the distance and a parameter that adjusts the probability for accepting. This parameter is called temperature in the simulated annealing framework (Kirkpatrick 1983). In the beginning the temperature is high, giving high acceptance probability to allow a wide search and easily escape sub-optimal solutions. As the process continuous it is more likely for the solution to be in an area around the global minimum and the temperature is decreased slowly for narrowing the search for the optimal solution. For each iteration, the algorithm checks a convergence criterion that must be met before the temperature is decreased. When the temperature goes towards zero the algorithm will mostly accept proposals that minimize the distance. The algorithm is stopped when a global convergence criterion is met. The whole workflow is illustrated in Fig. 3.

Figure 4 shows an illustration of a current fault set and a fault set where the selected fault has been replaced with a new proposed fault (highlighted in red). The proposed fault has different position and fault attributes than the fault it replaces. The rightmost panes in Fig. 4 show the corresponding total displacement fields for both fault sets. When a new fault is sampled, the displacement map is used as proxy for fault density, so the map will reflect the probability for where to place the fault. New proposed faults will then most often be suggested in regions with large displacement, which will greatly improve the convergence speed. Correspondingly, the algorithm will favour small or no faults in regions with low displacement. However, a region with high displacement may consists of many small faults or fewer larger faults.

The further details of the algorithm can be described as follows. A fault set of n number of faults is denoted as $f = \{f_i\}_1^n$, where d_{f_i} is the three-dimensional displacement field of the fault f_i. The total displacement field of fault set f then becomes $D_f = \Sigma_{i=1}^n d_{f_i}$. For calculation purposes the displacement fields are discretized and evaluated in m grid cells denoted as $d_{f,j}$ and $D_{f,j}$ where $j = 1, \dots, m$. The number of grid cells m should be high enough to reflect the complexity of the displacement map, but a large number of cells will also increase the run time.

The goal is to generate faults that minimize the distance between D_f and the input displacement map M. The comparison is done by the squared residual distance

$$L_f = \left| D_f - M \right|^2 = \Sigma_{j=1}^m \left(D_{f,j} - M_j \right)^2, \qquad (3)$$

where M_j is the discretized version of the input map. Thus, L_f is the object function of the algorithm and is in the following referred to as the distance.

Before running the algorithm, it must be initialized by the following steps:

1. Generate a fault set of n faults.
2. Calculate the total displacement field D_f of the fault set.
3. Determine initial value of the temperature T_0.

Sub-seismic faults are proposed, rejected and accepted in an iterative process as follows:

1. Compute the distance L_f for the current fault set using Eq. (3).
2. Propose the next step by:
    a. Randomly select one fault, f_k, in the fault set f and calculate the corresponding fault displacement field d_{f_k}.
    b. Sample a new (proposed) fault, f_p, with fault displacement field d_{f_p}.
    c. Compute a new distance L_p where the displacement of fault f_p is added and the displacement of fault f_k is subtracted from the total displacement field D_f. That is,

$$L_p = \Sigma_{j=1}^{m} \left(D_{f,j} + d_{f_p,j} - d_{f_k,j} - M_j\right)^2$$

3. Compute the acceptance criterion $\alpha = \exp(-\Delta/T_i)$, where $\Delta = L_p - L_f$ and T_i is the current temperature.
4. Draw u~U[0,1] from a uniform distribution and compare with the criterion:
    a. $\alpha \geq u$: The proposed fault is accepted. Replace f_k with f_p in f and update D_f accordingly.
    b. $\alpha < u$: The proposed fault is rejected.
5. If the end criterion is met for the current temperature (T_i):
    a. Lower the temperature according to an annealing schedule.

6. Terminate if the convergence end criterion is met, if not repeat from step 1.

The temperature is lowered according to a predefined annealing schedule. The schedule of Kirkpatrick (1983) is applied, where $T_{i+1} = sT_i$, and s is a predefined parameter that is less than 1. The algorithm should iterate a sufficient number of times before the temperature is lowered. For the current temperature (T_i) the number of accepts is counted, and the temperature is lowered if the number exceeds a predefined number N_a. Additionally, the temperature is also lowered if the total number of attempts exceeds N_T, where N_T should be several magnitudes larger than N_a. The schedule of lowering the temperature is similar to the suggested schedule in Tran (2007) and Masihi et al. (2012). The initial value T_0 should be determined based on the parameters of the current model, which in this case would mean the input parameters of Eqs. (1) and (2). Masihi et al. (2012) argues to select T_0 such that the acceptance ratio is around 0.95.

The end criterion for terminating the algorithm follows the suggestion of Kirkpatrick (1983). They suggested that if the desired number of acceptances (N_a) is not achieved at three successive temperatures, that is the number of iterations of three successive temperatures reaches N_T, then the algorithm should be stopped.

4. Testing on Synthetic Maps

To test the algorithm two-dimensional synthetic displacement and orientation maps are created as input. The maps are based on the Emerald field, that is a tutorial example of a faulted subsurface structure in the reservoir modelling software RMS (Roxar 2018). Figure 5 shows the faults and their location in the grid of the structural model. The size of the grid is about 7,700 m x 7,700 m x 750 m. See for example Qu et al. (2015) for further details. For illustration purposes, the synthetic displacement map is created only around the faults F2 and F3 that are highlighed in red in Fig. 5.

The synthetic displacement map is created by taking a linear trend that decreases away from the fault surface and adding Gaussian noise at random locations along the trend. Adding noise creates the effect of non-linear decreasing displacement in the damage zone and gives variability to the displacement map. For demonstration purposes it was prioritized to create a map that had this variability, rather than having the most geological realistic representation. Further, the trend has its maximum at the fault surface and reaches zero 800 meters away from the fault. The maximum is set to 20.5 meters, corresponding to the avereage displacement at the hanging wall and foot wall side of the faults. According to Torabi et al. (2019b) the extent of the damage zone depends on the fault displacement and would typically be between 5 and 80 meters for a fault with total displacement of about 40 meters, like F2 and F3. The larger extent of about 800 meters is selected to make the visual interpration of the different sub-seismic faults and the resulting displacement pattern easier. The synthetic displacement map is shown in Fig. 6 (left), representing the displacement in the damage zone around the faults. The solid black lines are the fault lines of the hanging wall and foot wall side of the fault when projected onto the two-dimensional map. Between the hanging wall and foot wall line, there is an area with no displacement due to the dipping of the faults and consequently sub-seismic faults are not allowed here. The synthetic orientation map is shown in Fig. 6 (right) where each point in the map is equal to the local strike of the closest fault, F2 or F3, repsectively.

To test the algorithm 700 sub-seismic faults is generated with displacement between 4 and 15 meter and a power-law exponent equal to 2 in Eq. (1). The number of faults is chosen so that the cumulative fault displacement prior to optimization ($\Sigma_{j=1}^{m} L_{f,j}$) is similar to the cumulative input displacement ($\Sigma_{j=1}^{m} M_j$). For the displacement versus length ratio a value of 0.01 for c_1 and 1.0 for c_2 in the Eq. (2) is used, which gives faults with lengths between 400 and 1,500 meters. The parameter c_3 in the fault length-height ratio is set to 2.0, and the parameter c_4 in the formula for the range is set to 0.3. The standard deviations $\sigma_1, \sigma_2, \sigma_3$ for the V_1, V_2 and V_3 distributions are set to 0.1, 0.1 and 0.2 respectively.

Further, the faults are vertical with dip angle 90 degree and strike values are drawn from a normal distribution where the mean value is taken from orientation map in Fig. 6 (right) with standard deviation equal to 10 degrees. The maps are discretized into 300x300 cells, which means that m in Eq. (3) is 90,000.

When setting up the simulated annealing parameters the start temperature T_0 is set to 10,000 and reduced by ten percent whenever updated, that means $T_i = 0.9T_{i-1}$. The temperature is updated when the number of accepted faults N_a reaches 200 or when the maximum number of attempts (proposing faults) N_T reaches 20,000. The algorithm is terminated when N_a is not reached for three consecutive temperatures.

Figure 7 shows the total displacement field of the initial set of faults where the locations of the faults are conditioned on the displacement map. The corresponding result after running the algorithm is shown in Fig. 8. The total displacement in Figs. 7 and 8 is shown both with and without the faults overlaid. When visually inspecting the results before and after running the optimization algorithm the position and orientation of the faults appear somewhat similar. The effect of the optimization is more evident in residual maps showing the difference between the total displacement and the synthetic displacement map. Figure 9 shows the residual of the total displacement at the initial step (left) and after the optimization (right). The figure clearly shows that the total displacement becomes closer to the synthetic map after running the algorithm.

Figure 10 shows the acceptance rate in percent and the squared distance L_f plotted for every thousand iteration. The criterion to stop the algorithm is reached after 175,000 iterations, which means that on average each fault has been proposed updated about 250 times. Figure 11 shows the evolution of the temperature during the course of the algorithm, reaching a final value of 8.6. Most of the improvements occurs during the first 30-40,000 iterations, where L_f drops to almost one fifth of its initial value. During the rest of the iterations the results slowly decreases until the end criterion is met. This behavior is typical for a simulated annealing process (Tran et al. 2006).

The effect of using different distributions to draw the maximum displacement of the sampled faults is also evaluated. Power-law, uniform, Gaussian and log-normal distributions are tested. The parameters for each distribution are listed in Table 1, and the distributions are plotted in Fig. 12. All distributions are truncated between 4 and 15 meters. The input data and settings (number of faults etc.) are the same as used in the example above. Table 2 list the cumulative displacement and squared residual distances (L_f) at the initial step and after the end criterion for the different distributions. The cumulative displacement is calculated by summing the discretized total displacement map, that is $\Sigma_{j=1}^{m} D_{f,j}$. From Table 2 it is seen that the squared residual distance at the initial step is much higher for uniform and Gaussian distributions, because these distributions will initially draw a higher number of larger faults than power-law and log-normal distributions. However, all four distributions reach about the same level of residual distance after the end criterion, with power-law achieving the lowest value. The shape of the resulting distributions reaches a similar skewed pattern where the mass is concentrated around the smaller faults. The cumulative input displacement, $\Sigma_{j=1}^{m} M_j$, is 159,580 m and in the table it is seen that the cumulative displacement of all four cases converges towards a similar value. These results lead to the conclusion that the simulated annealing algorithm is robust with regards to variations in the input distribution for drawing the sub-seismic fault displacement values.

5. Discussion

The presented method iteratively updates faults so that their total displacement matches with an input displacement map. The method is based on the following three required components: (1) A stochastic fault model must be used to generate faults with variability, (2) it must be possible to measure the displacement for each fault in the volume or along a horizon, and (3) a mechanism to add and remove single faults and their influence on the total displacement field is needed. The elliptic fault model of Hollund et al. (2002) is used as this is a flexible model for generating fault networks and calculating the faults' displacement field. It is however a simplistic representation of sub-seismic faults with the limitation that the maximum displacement is at the center of the fault. Other, more complicated sub-seismic fault models should also work well as long as the three required components are fulfilled. The same applies for more advanced interactions between faults, like evaluating truncations between sub-seismic faults when proposing and rejecting new faults. That would refine the displacement modelling and should be included in future developments of the model.

In the current fault model the same fault attribute relations (parameters in Eq. (2)) are used for all faults. Torabi and Berg (2011) investigates fault attribute relations where they suggest that the relations could change based on different level of displacement values. This is further discussed in Kolyukhin and Torabi (2012) for different types of faults and lithologies and in Kolyukhin et al. (2018) for faults in the Barents Sea. Incorporating these ideas into the model is straight forward, as the model first draws the displacement and then the subsequent attributes.

To better control the displacement distribution of the final fault set, deviations from a target fault displacement distribution like Eq. (1), could be included in the object function. That would prohibit the algorithm from only accepting small or large faults. If combined with a mechanism where the number of faults in the set is adjusted stochastically, the algorithm could also search for the optimum number of sub-seismic faults needed to replicate the displacement map. It is also straight forward to extend the algorithm to condition on multiple horizons or a full three-dimensional cube by letting the sum in Eq. (3) run over each horizon or over all cells in the cube.

Munthe et al. (1994), Hollund et al. (2002) and Maerten et al. (2006) addresses the problem of how to make sub-seismic fault networks consistent with observed horizons from seismic data. The presented method is a contribution along these lines, as it is searching for a fault set with total displacement similar to an input map. The input map could for example represent the depth variability of a horizon, observed from seismic or computed from a geomechamical model.

6. Conclusions

Simulated annealing is used to find the optimum position and fault attributes of sub-seismic faults in a three-dimensional volume to match input maps of displacement and fault strike orientation. The algorithm is demonstrated on synthetically created maps and it is shown that it quickly converges towards a set of sub-seismic faults giving total displacement and strike orientations close to the input maps. By numerical experiments, it is demonstrated that the convergence of the algorithm is robust with regards to using different fault size distributions.

It is suggested that the presented approach may be suitable when the aim is to create sub-seismic fault sets matching a specific displacement field and strike orientation maps. It would for example ensure good consistency between modelled sub-seismic faults and input maps from geomechanical model predictions or observations. From a more general perspective the presented approach contributes to the assessment of sub-seismic fault patterns that otherwise can be difficult to map from seismic or well data.

Acknowledgement

The authors thank Equinor for valuable discussions and for funding the development of the algorithm.

References

Bond CE (2015) Uncertainty in structural interpretation: Lessons to be learnt. J. Struct. Geol. 74:185-200. https://doi.org/10.1016/j.jsg.2015.03.003

Cherpeau N, Caumon G, Lévy B (2010) Stochastic simulations of fault networks in 3D structural modelling. Comp. Rend. Geoscience 342:687–694. https://doi.org/10.1016/j.crte.2010.04.008

Damsleth E, Sangolt V, Aamodt G (1998) Sub-seismic Faults Can Seriously Affect Fluid Flow in the Njord Field off Western Norway - A Stochastic Fault Modeling Case Study. SPE Paper 49024, 10 p. https://doi.org/10.2118/49024-MS

Georgsen F, Røe P, Syversveen AR, Lia O (2012) Fault displacement modelling using 3D vector fields. Computational Geosciences 16:247–259. https://doi.org/10.1007/s10596-011-9257-z

Gibson JR, Walsh J, Watterson J (1989) Modelling of bed contours and cross-sections adjacent to planar normal faults. Structural Geology 11:317-328. https://doi.org/10.1016/0191-8141(89)90071-0

Gillespie P, Casini G, Iben H, O'Brien JF (2017) Simulation of subseismic joint and fault networks using a heuristic mechanical model. In Ashton, M., Dee, S.J., Wennberg, O.P. (eds) Subseismic-Scale Reservoir Deformation, The Geol. Soc. London, Spec. Publ. 459:177-190 https://doi.org/10.1144/SP459.6

Godefroy G, Caumon G, Laurent G, Bonneau F (2019) Structural Interpretation of Sparse Fault Data Using Graph Theory and Geological Rules. Math. Geosci. 51:1091-1107. https://doi.org/10.1007/s11004-019-09800-0

Gong L, Liu B, Fu X et al (2019) Quantitative prediction of sub-seismic faults and their impact on waterflood performance: Bozhong 34 oilfield case study. J. Petr. Sci. Eng. 172:60-69. https://doi.org/10.1016/j.petrol.2018.09.049

Hollund K, Mostad P, Nielsen BF et al (2002) Havana – a fault modeling tool. In: Hydrocarbon seal quantification, Norwegian petroleum society conference. NPF Spec Pub, vol 11. Elsevier, Amsterdam. https://doi.org/10.1016/S0928-8937(02)80013-3

Kim Y, Sanderson DJ (2005) The relationship between displacement and length of faults: A review. Earth-Science 68:317-334. https://doi.org/10.1016/j.earscirev.2004.06.003

Kirkpatrick S, Gelatt Jr, CD and Vecchi MP (1983) Optimization by Simulated Annealing. Science 220:671-680. https://doi.org/10.1126/science.220.4598.671

Kolyukhin D, Torabi A (2012) Statistical analysis of the relationships between faults attributes. Journal of Geophysical Research: Solid Earth. 117(B05406). https://doi.org/10.1029/2011JB008880

Kolyukhin D, Torabi A, Libak A, Alaei B, Khachkova T (2018). Statistical Analysis of Displacement and Length Relation for Normal Faults in the Barents Sea. Geosciences, 8(11):421. https://doi.org/10.3390/geosciences8110421

Maerten L, Gillespie P, Daniel J-M (2006) Three-dimensional geomechanical modeling for constraint of subseismic fault simulation. AAPG Bulletin 90:1337-1358. https://doi.org/10.1306/03130605148

Mahmoodpour S, Masihi M (2016). An improved simulated annealing algorithm in fracture network modeling. Journal of Natural Gas Science and Engineering 33:358-550. https://doi.org/10.1016/j.jngse.2016.05.056

Masihi M, Sobhani M, Al-Ajm, A, Al-Wahaib, Y, Al Wahaibi T (2012). A physically-based three dimensional fracture network modeling technique. Scientia Iranica 19:594-604 https://doi.org/10.1016/j.scient.2012.01.008

Munthe K, Holden L, Mostad P, Townsend C (1994) Modelling Sub-seismic Fault Patterns using a Marked Point Process. In: ECMOR IV, 4th European Conference on Mathematics of Oil Recovery, Røros, Norway, SPE 49024, 295-304. https://doi.org/10.3997/2214-4609.201411151

Ponting DK (1989) Corner point geometry in reservoir simulation. ECMOR I - 1st European Conference on the Mathematics of Oil Recovery, Cambridge, UK. https://doi.org/10.3997/2214-4609.201411305

Qu D, Røe P, Tveranger J (2015) A method for generating volumetric fault zone grids for pillar gridded reservoir models. Computers and Geosciences 81:28-37. https://doi.org/10.1016/j.cageo.2015.04.009

Roxar, 2018. RMS 11.0.1 User Guide. Roxar Software Solutions, Stavanger, Norway

Roche V, Camanni G, Childs C et al (2021) Variability in the three-dimensional geometry of segmented normal fault surfaces. Earth-Science Reviews 216:103523 https://doi.org/10.1016/j.earscirev.2021.103523

Walsh JJ, Watterson J (1988). Analysis of the relationship between displacements and dimensions of faults. Journal of Structural Geology 10:239-247. https://doi.org/10.1016/0191-8141(88)90057-0

Torabi A, Alaei B, Libak A (2019a) Normal fault 3D geometry and displacement revisited: Insights from faults in the Norwegian Barents Sea. Marine and Petroleum Geology 99. 135-155. https://doi.org/10.1016/j.marpetgeo.2018.09.032

Torabi A, Berg SS (2011) Scaling of fault attributes: A review. Marine and Petr. Geol. 28:1444-1460. https://doi.org/10.1016/j.marpetgeo.2011.04.003

Torabi A, Ellingsen TSS, Johannessen MU, Alaei B, Rotevatn A, Chiarella D (2019b) Fault zone architecture and its scaling laws: where does the damage zone start and stop? Geol. Soc. London, Spec. Publ. 496:99-124. https://doi.org/10.1144/SP496-2018-151

Tran N (2007). Simulated annealing technique in discrete fracture network inversion: optimizing the optimization. Computational Geosciences 11:249-260. https://doi.org/10.1007/s10596-007-9049-7

Tran N, Chen Z, Rahman S (2006). Integrated conditional global optimisation for discrete fracture network modelling. Computers & Geosciences, 32:17-27. https://doi.org/10.1016/j.cageo.2005.03.019

Yielding G, Walsh J, Watterson J (1992) The prediction of small-scale faulting in reservoirs. First Break 10:449-460. https://doi.org/10.3997/1365-2397.1992023

Figure Captions

Fig. 1 Three-dimensional grid deformed by an elliptic fault

Fig. 2 Example of using laterally varying maps in stochastic modelling of sub-seismic faults. To the left the faults are positioned at random in the volume and to the right the faults' position and orientation are picked according to underlying density and orientation maps

Fig. 3 Flow diagram of the workflow

Fig. 4 Fault set with 9 faults (left). Current fault fault selected (top center, red) and an alternative fault sampled (bottom center, red). To the right is the total displacement fields for current (top) and proposed (bottom) fault sets

Fig. 5 Structural model of the Emerald field dataset from RMS (Roxar 2018) with faults F2 and F3 highlighted as red

Fig. 6 The synthetic displacement map (left) and the strike orientation map (right). The colors represent displacement (left) and degree of orientation (right). Each map is overlaid with hanging wall and foot wall lines for the two faults F2 and F3 from Fig. 5

Fig. 7 Total displacement field from the 700 generated sub-seismic faults at the initialization step with (left) and without (right) the sub-seismic faults overlaid as black lines

Fig. 8 Total displacement field from the 700 sub-seismic faults after running the algorithm with (left) and without (right) the sub-seismic faults overlaid as black lines

Fig. 9 The residual maps at the initialization step (left) and after running the algorithm (right)

Fig. 10 The acceptance rate of the proposed faults in percent (orange) and the evolution of the objective function L_f (blue) plotted for every thousand iteration

Fig. 11 Evolution of annealing temperature (logarithmic scale) versus iteration

Fig. 12 Distributions used for drawing maximum displacement of sub-seismic faults. All distributions are truncated below 4 and above 15 meters

Table Captions

Tab. 1 Distributions used for drawing maximum displacement of the sub-seismic faults. All distributions are truncated below 4 and above 15 meters. SD denotes the standard deviation of the distribution

Tab. 2 The cumulative displacement and squared residual distance (L_f) at the initial step and after the end criterion when using the different distributions in Table 1 to draw the maximum displacement of the faults. All values are in meters

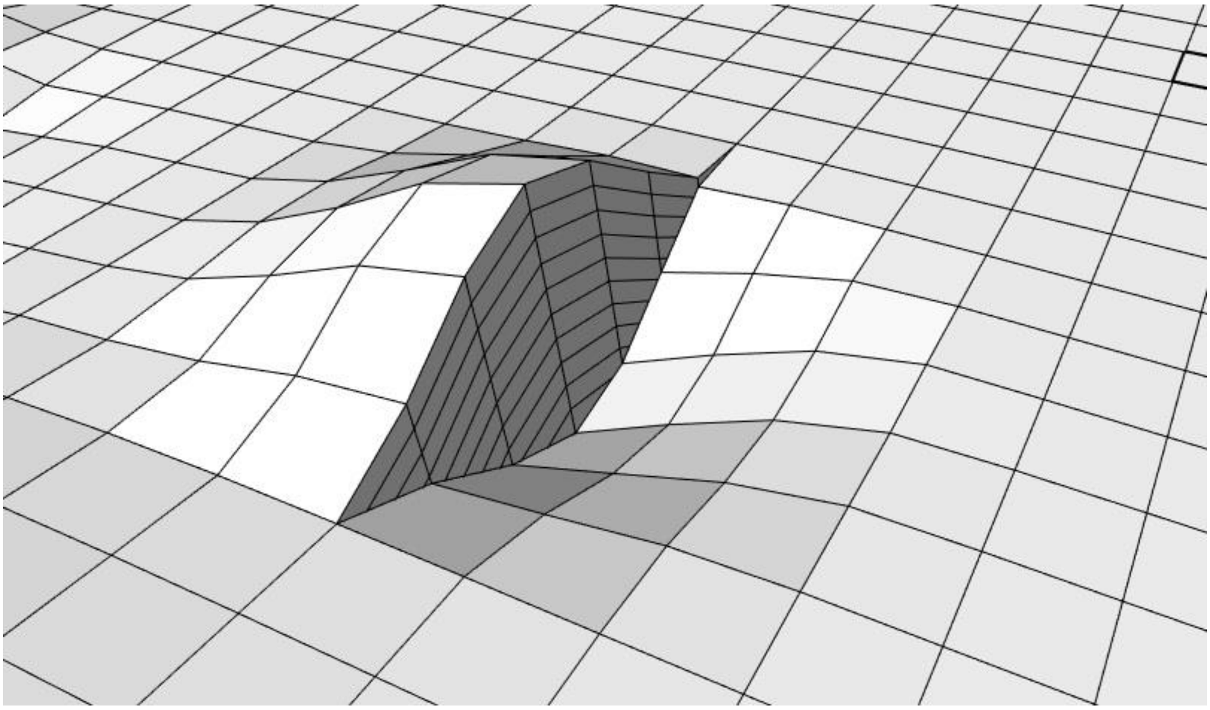

Figure 1

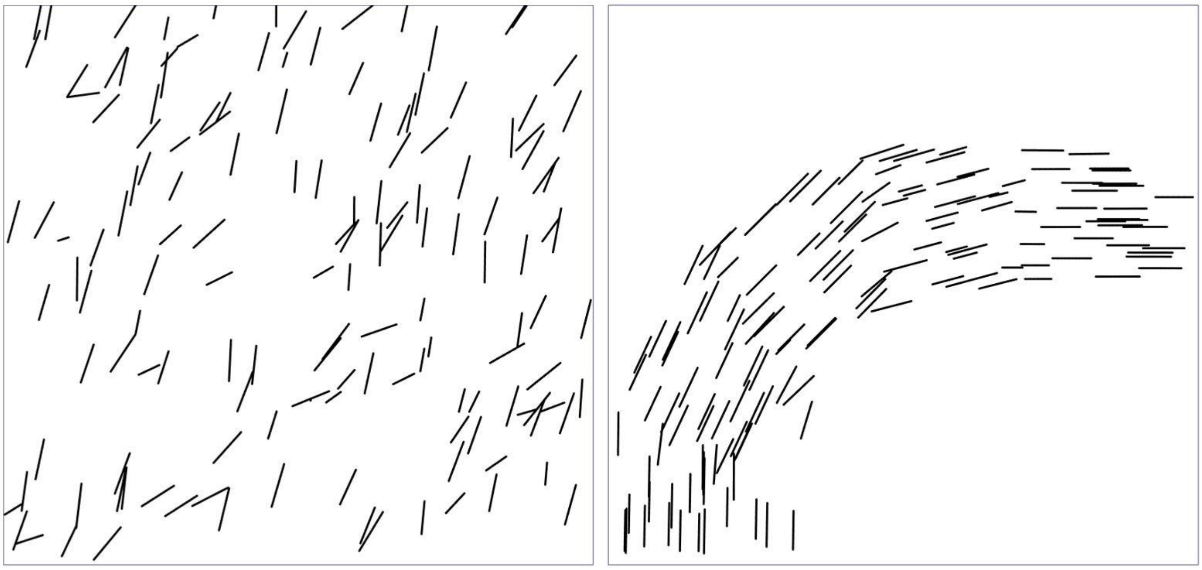

Figure 2

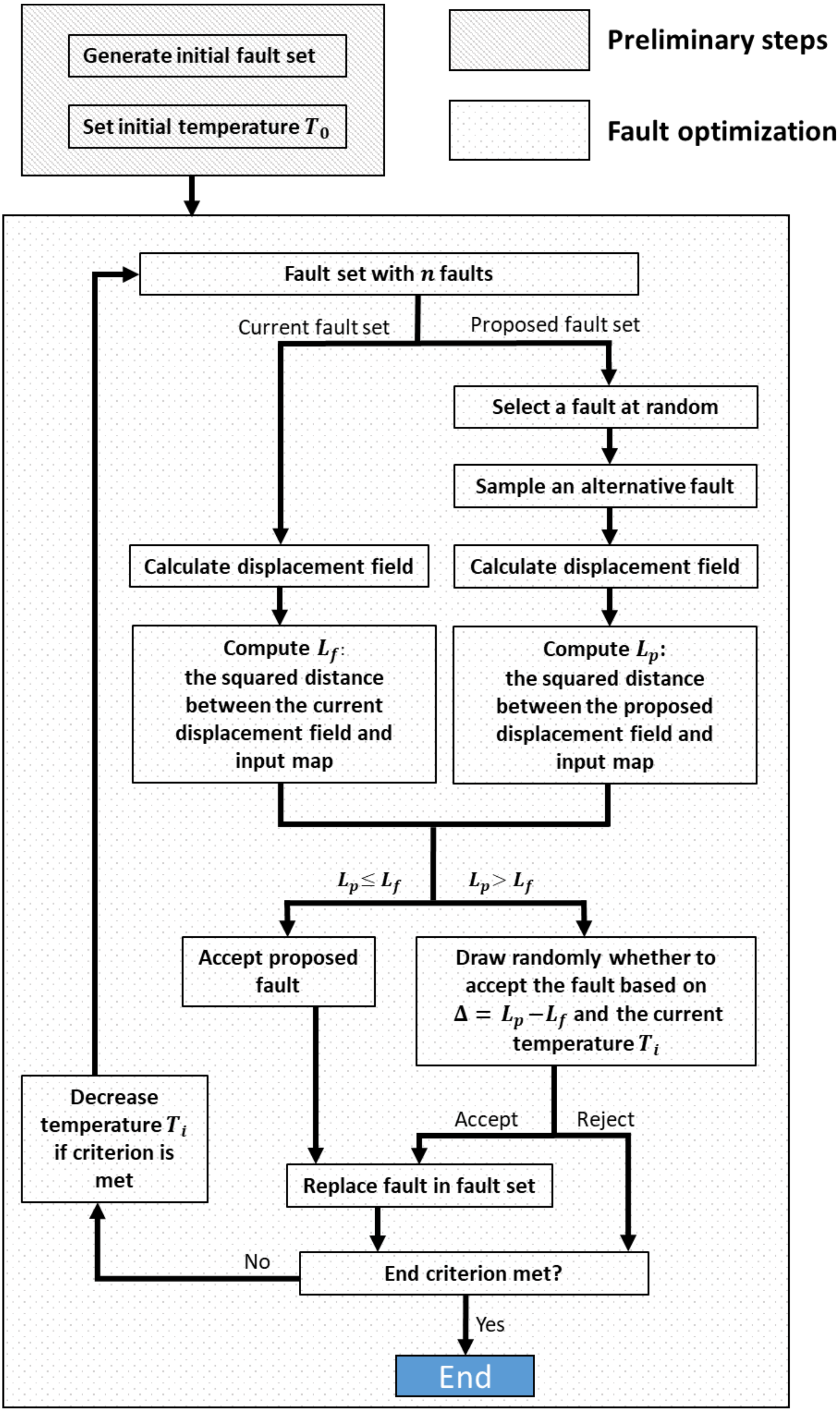
Generate initial fault set
Set initial temperature T_0
Preliminary steps
Fault optimization
Fault set with n faults
Current fault set
Proposed fault set
Select a fault at random
Sample an alternative fault
Calculate displacement field
Calculate displacement field
Compute L_f: the squared distance between the current displacement field and input map
Compute L_p: the squared distance between the proposed displacement field and input map
$L_p \leq L_f$
$L_p > L_f$
Accept proposed fault
Draw randomly whether to accept the fault based on $\Delta = L_p - L_f$ and the current temperature T_i
Accept
Reject
Decrease temperature T_i if criterion is met
Replace fault in fault set
No
End criterion met?
Yes
End

Figure 3

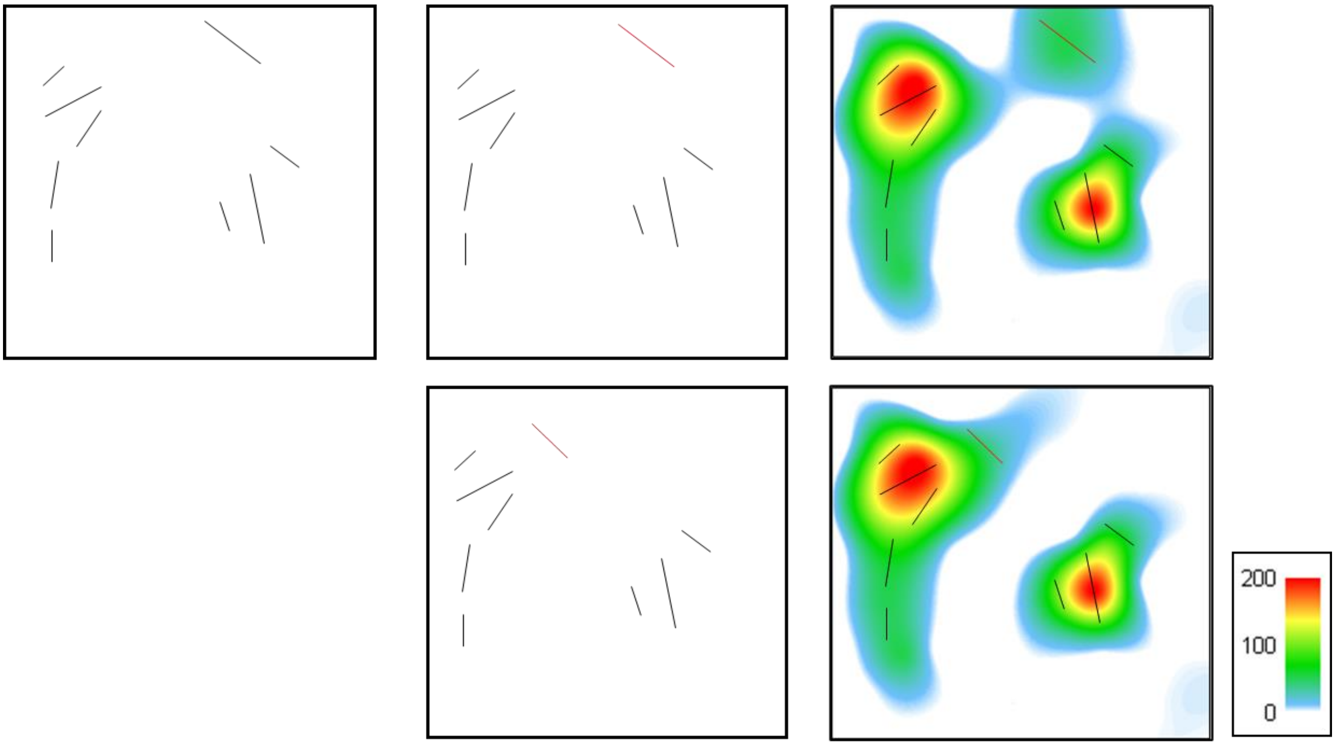

Figure 4

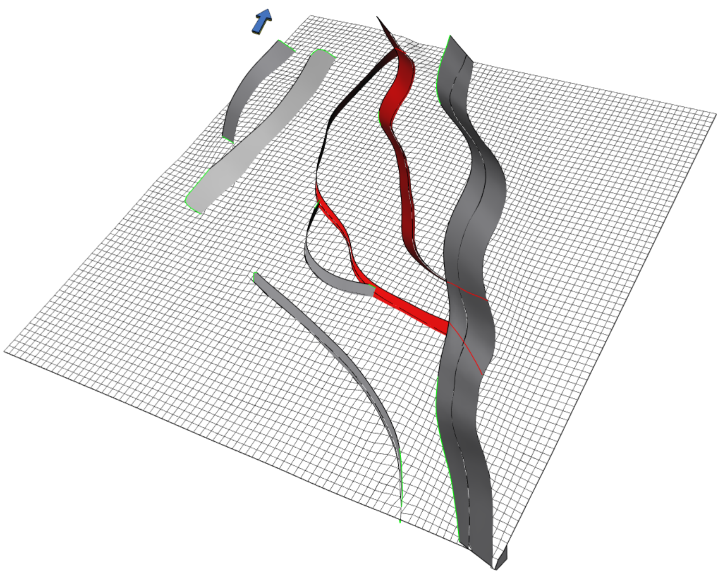

Figure 5

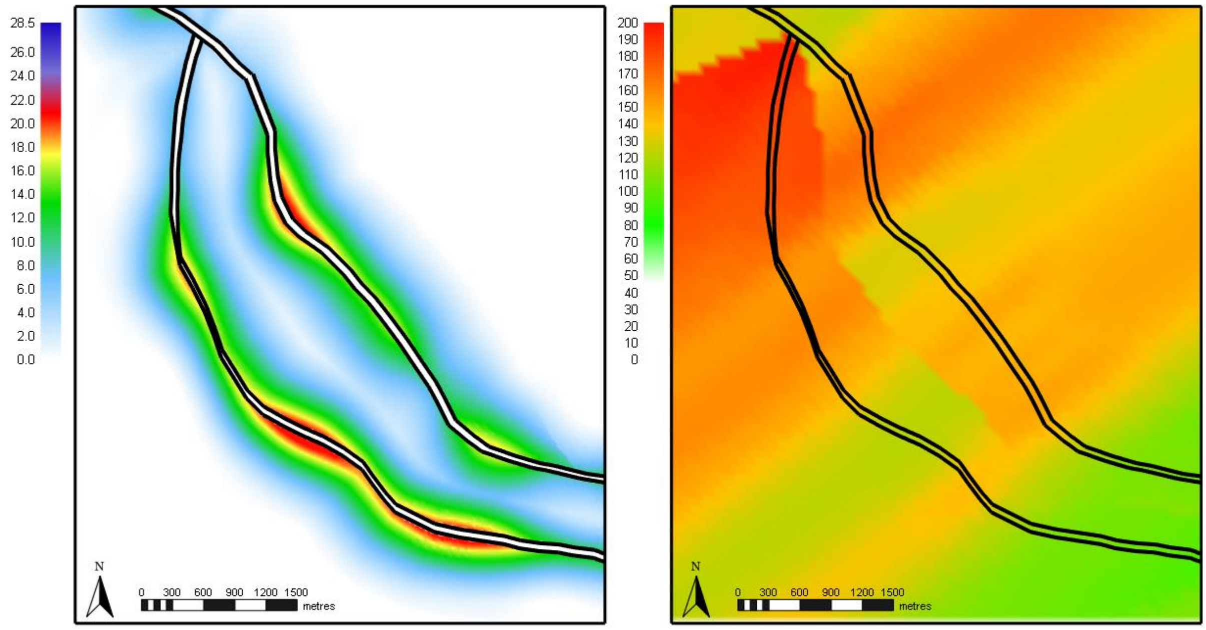

Figure 6

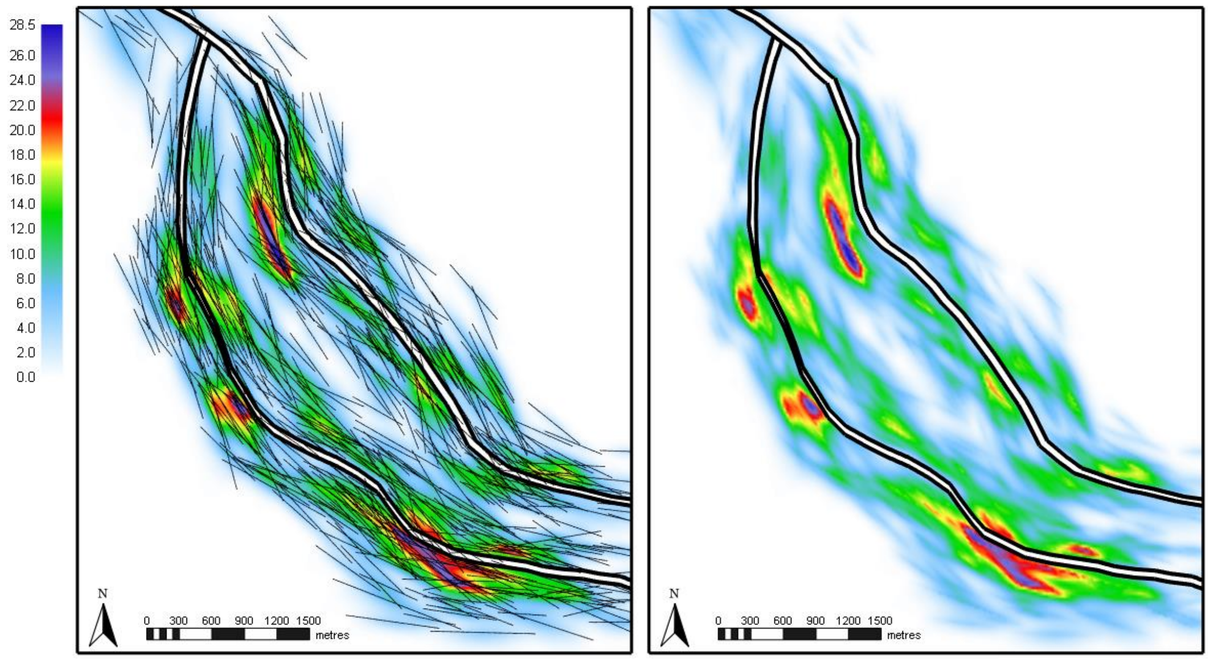

Figure 7

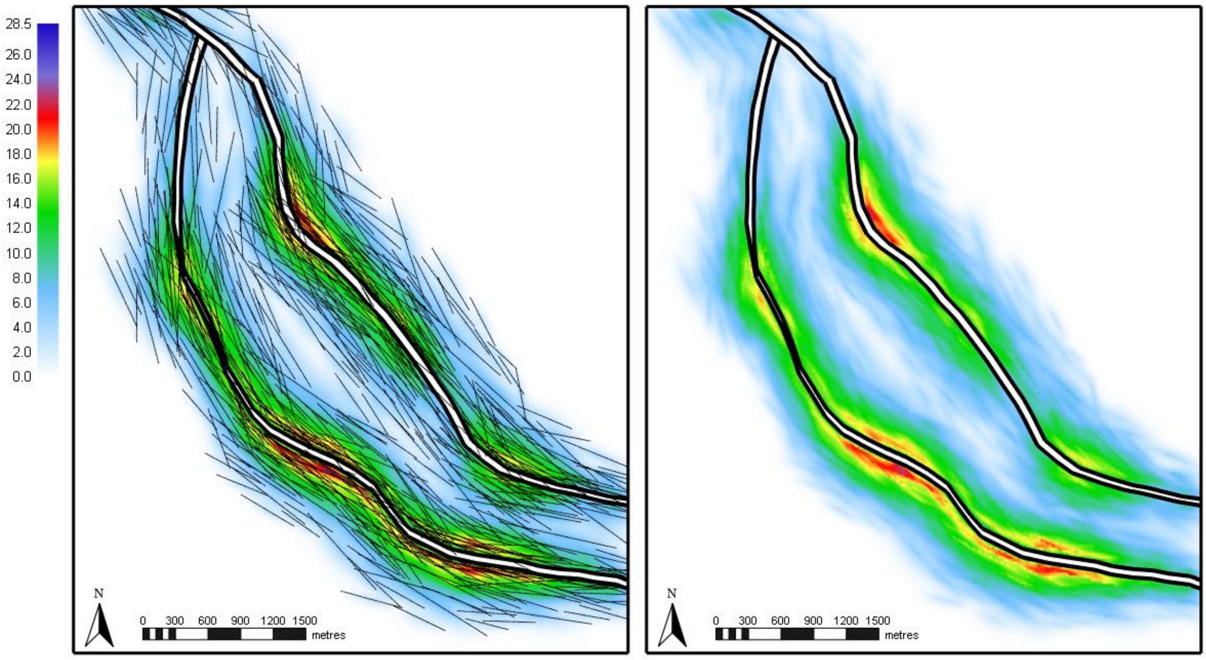

Figure 8

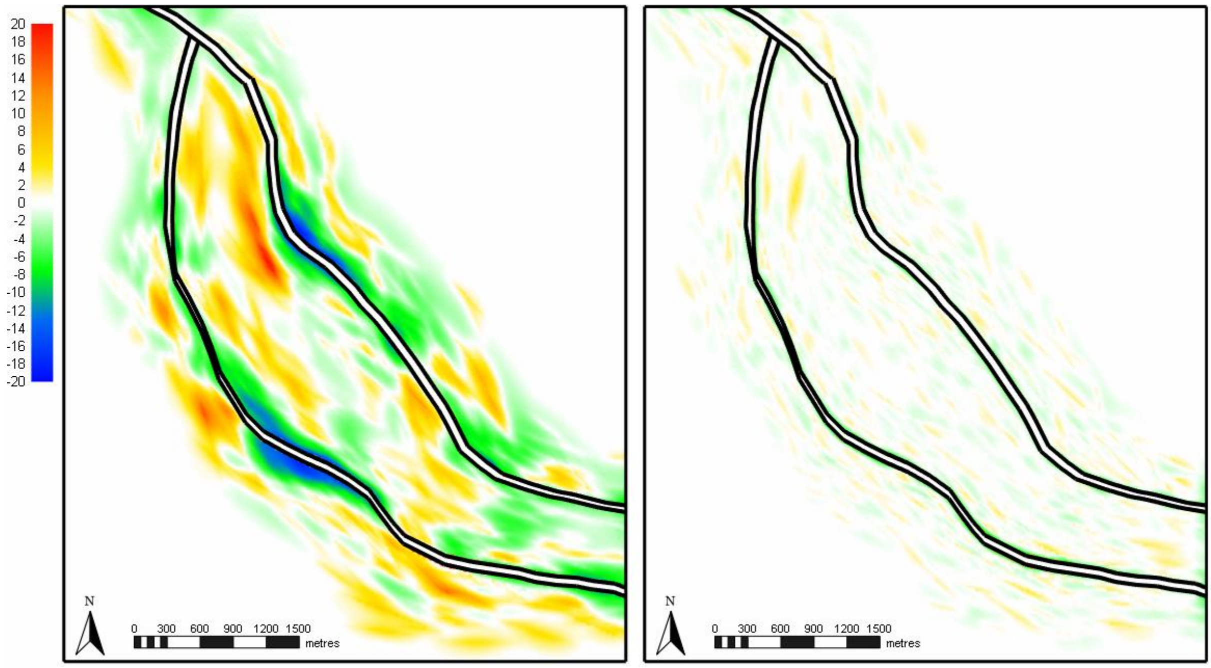

Figure 9

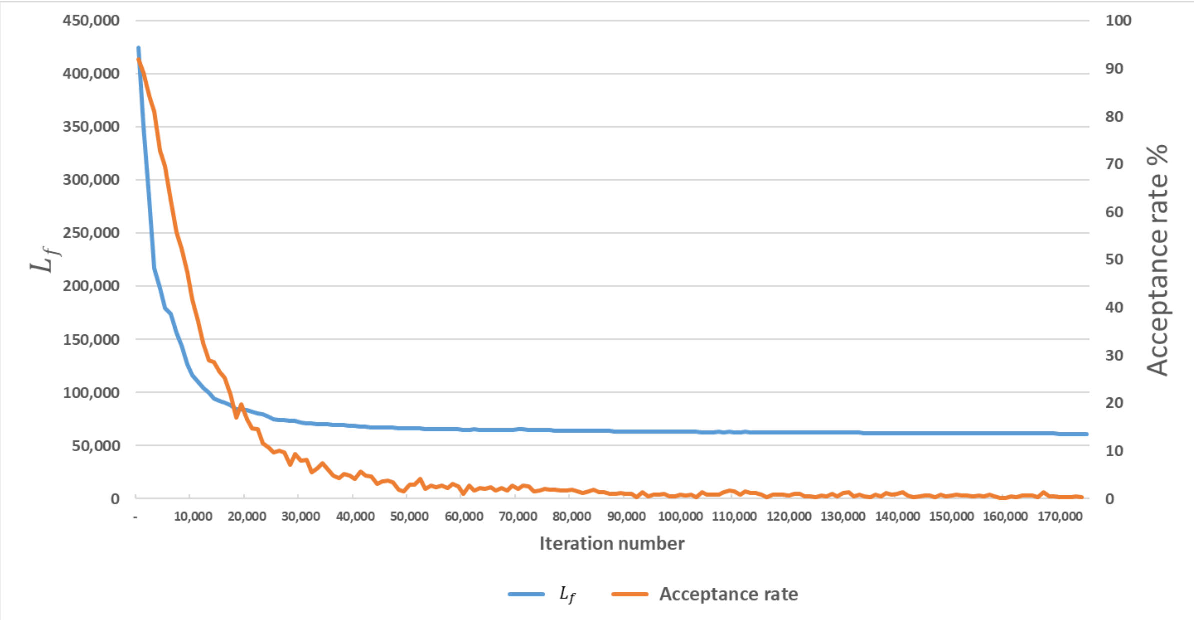

Figure 10

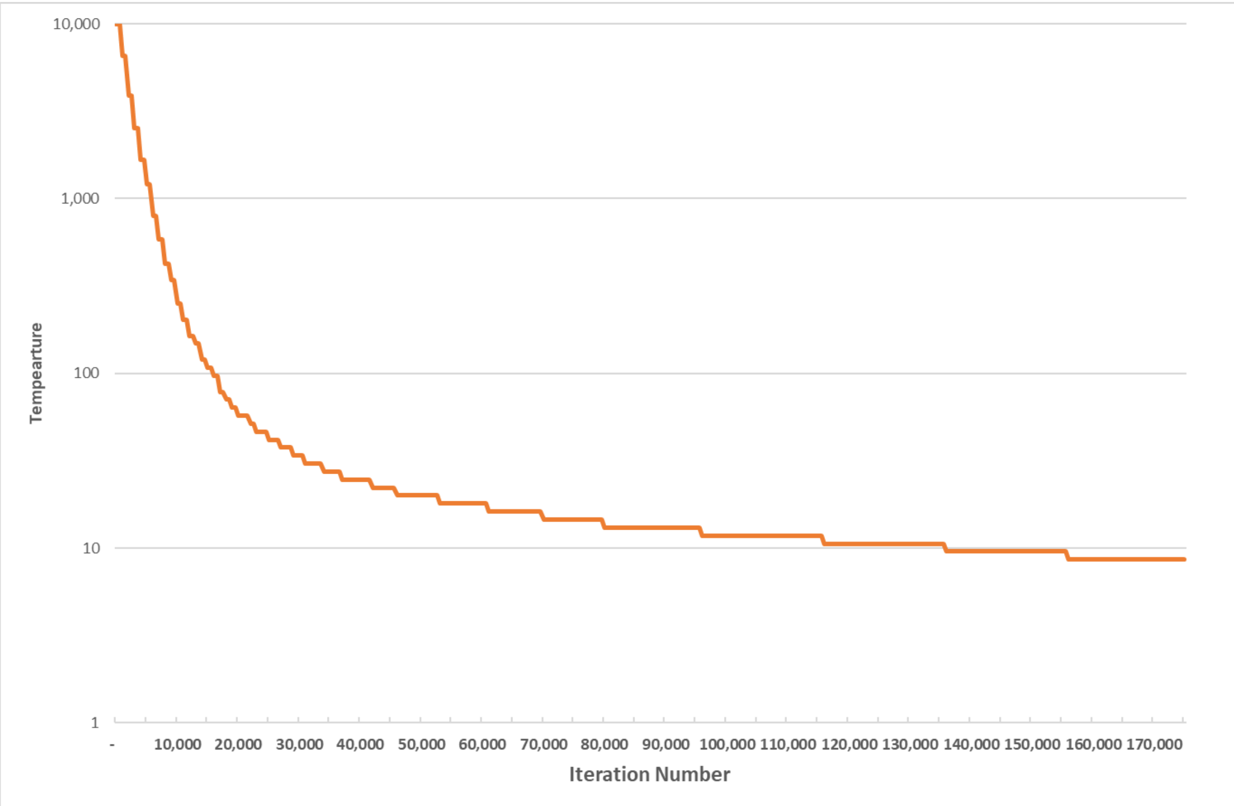

Figure 11

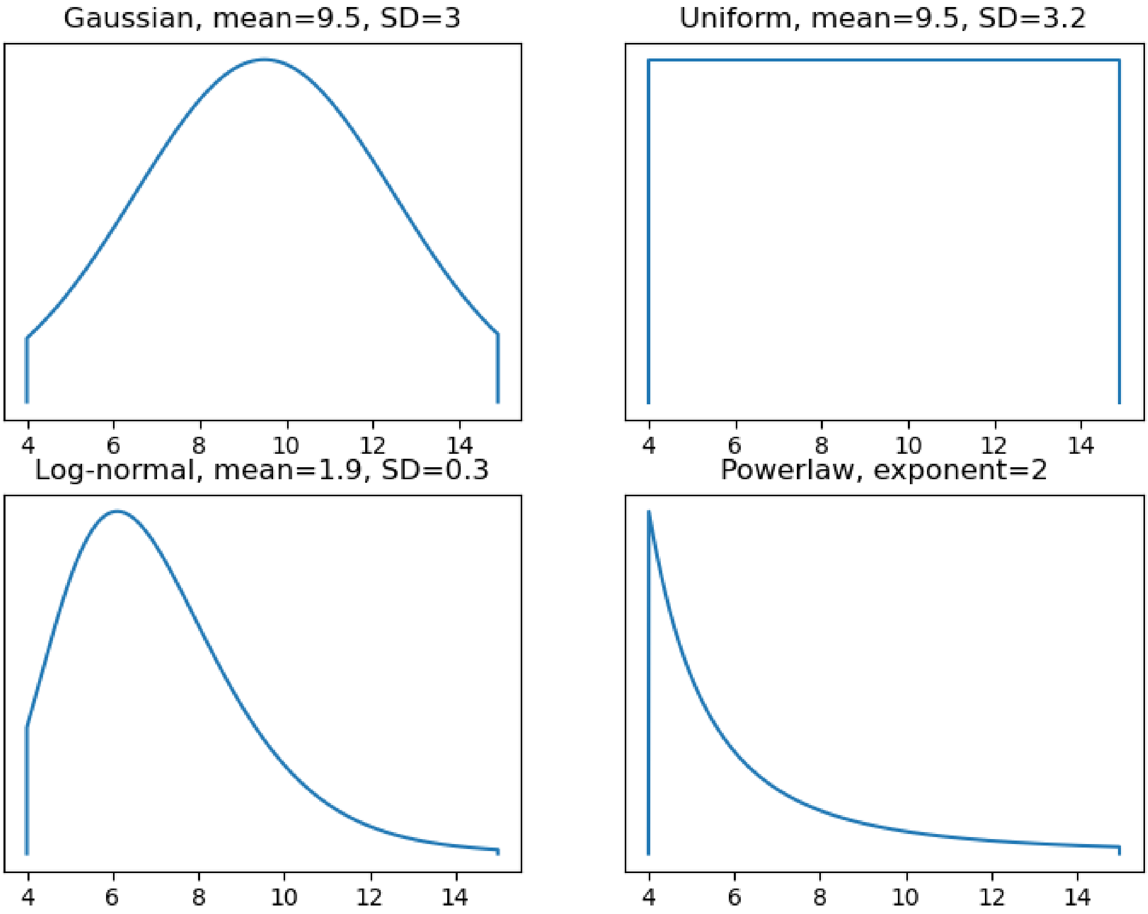

Gaussian, mean=9.5, SD=3
Uniform, mean=9.5, SD=3.2
Log-normal, mean=1.9, SD=0.3
Powerlaw, exponent=2
4
6
8
10
12
14

Figure 12

Distribution	Parameters
Power-law	Power-law exponent = 2
Uniform	Mean = 9.5, SD = 3.2
Gaussian	Mean = 9.5, SD = 3
Log-normal	Mean = 1.9, SD = 0.3

Table 1

Distribution	Initial step		After end criterion	
	Cumulative displacement	Cumulative residual	Cumulative displacement	Cumulative residual
Power-law	152,561	424,361	158,224	61,103
Uniform	447,446	5,466,440	159,920	64,348
Gaussian	413,608	4,329,780	160,292	66,581
Lognormal	174,017	481,200	157,927	63,711

Table 2